A dynamic model of the jump-to phenomenon during AFM analysis

Journal Item

A dynamic model of the jump-to phenomenon during AFM analysis

James Bowen,[1,*] David Cheneler[2]

[1] School of Chemical Engineering, The University of Birmingham, Edgbaston, Birmingham, B15 2TT, UK

[2] School of Mechanical Engineering, The University of Birmingham, Edgbaston, Birmingham, B15 2TT, UK

* To whom correspondence should be addressed

Email: j.bowen.1@bham.ac.uk

Abstract

The measurement of the physical properties of surfaces on the nanoscale is a long-standing problem, and the atomic force microscope (AFM) has enabled the investigation of surface energies and mechanical properties over a range of length scales. The ability to measure these properties for softer materials presents a challenge when interpreting data obtained from such measurements, in particular because of the dynamics of the compliant AFM microcantilever. This work attempts to better understand the interaction between an AFM tip and samples of varying elastic modulus, in the presence of attractive van der Waals forces. A theoretical model is presented in which the dynamics of the approach of an atomic force microscope cantilever tip towards a surface, prior to and during the van der Waals-induced jump-to phenomenon, are included. The cantilever mechanics incorporates the motion of the air through which the cantilever moves, the acceleration, inertia and torque of the cantilever, and the squeezing of the fluid between the cantilever tip and the surface, leading to elastohydrodynamic lubrication and deformation of the substrate. Simulations of the cantilever approach are compared to measurements performed using an atomic force microscope, and the effect of cantilever drive velocity is investigated. Cantilevers presenting (i) spherical colloid probe tips and (ii) pyramidal tips are employed, and substrates exhibiting Young's moduli of 3 MPa, 500 MPa, and 75 GPa are measured. The analysis presented could be extended to enhance understanding of dynamic phenomena in micro/nanoelectromechanical systems such as resonators and microrheometers, particularly those which contain soft materials and also where surface interactions are important.

Keywords

atomic force microscopy, jump-to, colloid probe, compliant, surface, cantilever, van der Waals

1. Introduction

The atomic force microscope (AFM)[1] has revolutionised the way in which researchers can directly probe the interaction forces between two surfaces. Instrument configurations afford the possibility of investigating nanoscale interaction between two materials of interest, under gaseous environments, aqueous and organic liquids, or vacuum conditions. The materials are brought towards one another using a piezoelectric translation stage, and the interaction force between the surfaces is measured by monitoring the deflection of a microfabricated cantilever, to which one of the two materials is attached, often in the form of a colloid probe.[2] Usually it is the adhesive interaction force required to separate the two surfaces which is of interest to researchers, and this is generally termed the "pull-off" force. There is often significant insight to be gained from interpreting the interaction behaviour upon the approach of the two surfaces, a process which often ends with a "jump-to" or "snap-in" event, which occurs when the gradient of any attractive forces between the surfaces exceeds the compliance of the AFM cantilever. The attractive forces typically consist of van der Waal, whilst electrostatic interactions can be either repulsive or attractive, depending upon the surface charges of the two bodies being brought together. There have been numerous publications which addressed the jump-to phenomenon, either in full or in part. Some of the earliest research which considered AFM jump-to events was performed by Butt,[3] who studied forces experienced by the AFM tip in electrolyte solutions. This was followed by a detailed study by Weisenhorn *et al*.[4] which considered the nature of the "jump-to" and "pull-off" events for a range of surfaces and liquid media.

A number of studies have considered the approach of an AFM cantilever, modified with a colloid probe tip, towards a deformable interface such as an air bubble[5-6] or oil droplet.[7] In both situations the surface was found to deform upon the cantilever approach, during which time a repulsive force was applied to the cantilever, due to squeezing of the fluid film present between the colloid probe and the deformable surface. The approach usually ended in the colloid probe being engulfed by the bubble or droplet, unless either dissolved salt, surfactant or polymer was used to prevent this from occurring. Gady *et al*.[8] studied the jump-to phenomenon for polystyrene microparticles against highly-oriented pyrolytic graphite, arriving at expressions which were useful for estimating the jump-to distance when electrostatic forces were important and also when they were not. Cappella and Dietler[9] showed that the jump-to distance is inversely proportional to the cantilever spring constant, modelling the tip-sample interaction using a Lennard-Jones potential. Attard *et al*.[10] considered the approach of a cantilever oscillating at its first resonant frequency towards a surface, identifying those regimes in which inertia is significant. Attard and Gillies[11] also considered the approach of a colloid probe towards a deformable viscoelastic droplet, fitting a theoretical model to experimental data in order to estimate the moduli and relaxation time of the material. Butt and Stark[12] examined the jump-to phenomenon for thin liquid layers, attempting to estimate liquid thin film thickness from the acquired jump-to data. Das *et al*.[13] explored the jump-to phenomenon as a means to estimate the Hamaker constant, utilising a model which incorporated a simple expression for the dynamic motion of the cantilever. There has also been a substantial review by Attard[14] which summarises many of these results.

A number of works which considered the attractive forces between two deformable spheres have been published. For example Parker and Attard[15-16] considered theoretically the quasi-static deformation of spherical elastic surfaces due to both attractive and repulsive surface forces, including van der Waals interactions, electrical double layer interactions, and solvation forces, comparing the results to Hertz,[17] Derjaguin-Muller-Toporov,[18] and Johnson-Kendall-Roberts[19] theories of contact. Attard[20] then considered theoretically the deformation of viscoelastic particles, reporting that hysteresis between the loading and unloading curves increased with increasing driving velocity.

In this work we investigate the effect that dynamic forces and substrate compliance have on the jump-to distance for measurements between surfaces in air. The fixed end of the cantilever is driven towards the substrate at a

constant velocity, and the cantilever is not oscillating in the vertical direction at its resonant frequency. We consider a sphere-on-flat configuration, in which either (i) a spherical colloid probe or (ii) pyramidal tip is attached or fabricated near to the end of the approaching cantilever beam. The tip is assumed to be made of SiO_2, as this is a common material used for spherical colloid probes, and pyramidal tipped cantilevers are usually manufactured from Si, which presents a SiO_2 outer surface. The cantilever mechanics are thoroughly examined, taking into account the motion of the air through which the cantilever moves, the acceleration, inertia and torque of the cantilever, and the squeezing of the air between the sphere and the flat surface. Contact mode AFM measurements of the jump-to distance are performed over four orders of magnitude of cantilever drive velocity, employing (i) a spherical colloid probe tip and (ii) a pyramidal tip, versus (a) a glass substrate, (b) a poly(propylene) substrate and (c) a poly(dimethylsiloxane) substrate. Experimental results are compared to theoretical calculations and where there are differences between the theory and the experiment, possible causes are suggested and explored.

2. Theory

2.1 van der Waals force, F_V

Israelachvili defined the van der Waals force between a sphere and a flat surface as:[21]

$$F_{VS} = \frac{AR}{6D^2} \quad (1)$$

where A is the Hamaker constant for the two materials, R is the sphere radius, D is the separation distance between the closest point of the sphere and the flat surface, and $R \gg D$. Similarly, Argento and French[22] derived an analogous expression for the van der Waals force between a cone apex and a flat surface:

$$F_{VC} = \frac{A\tan\phi[D\sin\phi+R\sin\phi+R\cos(2\phi)]}{6\cos\phi(D+R-R\sin\phi)^2} \quad (2)$$

where ϕ is the angle of the cone from the surface normal. A cone apex is a suitable model for the end of an AFM tip, which is typically pyramidal or conical in shape away from the tip. In contrast a sphere is a suitable model geometry for a colloid probe, which is usually a spherical particle with radius in the range 1-20 µm attached near to the apex of a rectangular AFM cantilever. Schematics of a pyramidal cantilever tip and beam are shown in Fig. 1. The cantilever width, w, is typically 30-40 µm, whilst the length, L, is typically 100 µm or greater.[2] The distance between the end of the beam and the centre of mass of the tip is denoted dL. The cone apex is also represented by a sphere of radius R. Hereafter, the force due to the van der Waals force is referred to as F_V, which applies to either a pyramidal tip or a spherical colloid probe tip.

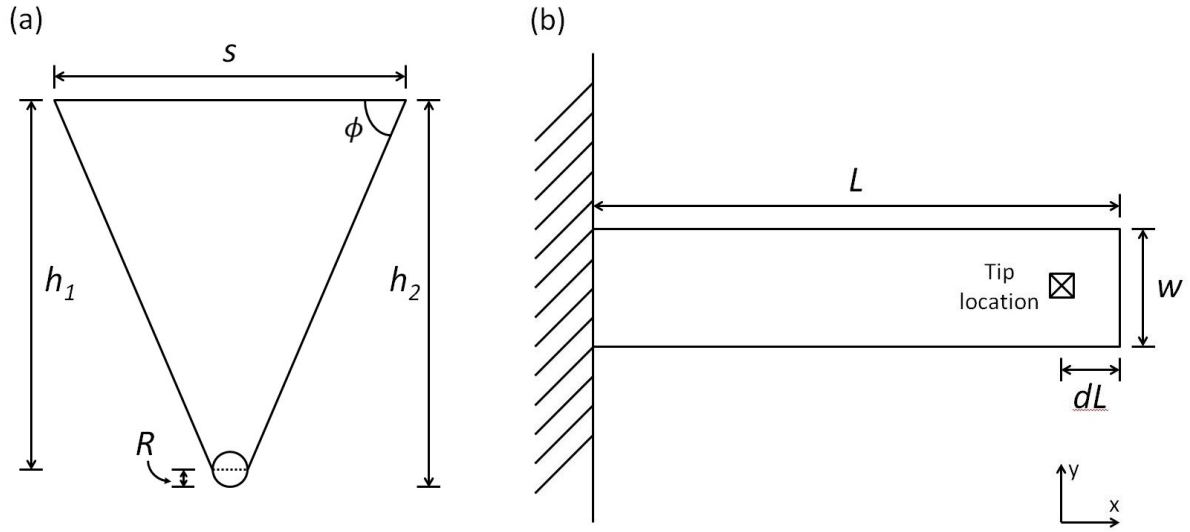

Fig. 1 Schematic showing (a) pyramidal tip geometry and (b) dimensions of rectangular cantilever beam

2.2 Force applied to tip due to fluid squeezing, F_{ST}

Whilst approaching the substrate surface, which is initially flat, the motion of the cantilever will be impeded due to viscous dissipation caused by the squeezing of the fluid entrained between the cantilever and tip and the flat countersurface. In the case considered here, the fluid under consideration is air at standard temperature and

pressure. Therefore the squeeze flow force due to the fluid between the AFM tip and the flat surface acts on the bottom of the tip and is simply described as:[23]

$$F_{ST} = \frac{6\pi\mu_{EFF}R^2\dot{D}_T}{D} \quad (3)$$

Here $\dot{D}_T$ is the tip velocity and μ_{EFF} is the effective viscosity of the fluid. Assuming the fluid to be air under ambient conditions, the effective air viscosity differs from the normal air viscosity because at small gaps the air becomes compressed and therefore the continuum approximation usually employed in squeeze flow becomes less applicable. To deal with the compression, the dynamic viscosity is modified to give:[24]

$$\mu_{EFF} = \frac{\mu}{1+9.638\left(\frac{\ell}{D}\right)^{1.159}} \quad (4)$$

Here $\mu = 1.983 \times 10^{-5}$ kg/m.s, which is the viscosity of air at standard temperature and pressure, and $\ell = 8 \times 10^{-8}$ m, which is the mean free path length of air at standard temperature and pressure. The quantity ℓ/D is equal to the Knudsen number, Kn, which is defined here as the ratio of the mean free path length to the gap between the moving object and the flat surface.

2.3 Gap between tip and surface due to elastohydrodynamic lubrication

One effect of a compliant substrate is due to elastohydrodynamic lubrication caused by the constrained fluid between the tip and substrate, as discussed in §2.2. Fig. 2 shows the system geometry under consideration in this work. The sphere, of radius R, represents either the hemispherical end of a pyramidal tip or a colloidal particle attached at the end of a cantilever. As the sphere approaches the substrate surface, the air between the sphere and substrate is squeezed, leading to a deformation of the substrate surface, described algebraically as $u(r,z)$. This effect is termed elastohydrodynamic lubrication (EHL) and occurs due to the compliance of the substrate. If such an effect were to occur, the jump-to distance measured would be greater than the jump-to distance that would have been measured were EHL not present in the system.

The hydrodynamic pressure profile due to squeeze flow can be found by solving the well-known lubrication equation to yield:[25]

$$p(r) = \frac{3\mu_{EFF}R\dot{D}_T}{\left[D+\frac{r^2}{2R}+u(r,0)\right]^2} \quad (5)$$

where $u(r,0)$ is the deformation of the substrate surface underneath the lowest point of the tip, and r is the is the radial distance from the centre of the tip. Eq. 5 can be integrated directly to find the force applied to the tip due to fluid squeezing, F_{ST}, and this tends to Eq. 3 when the surface deformation is negligible. For the case where the surface deformation cannot be considered negligible, $u(r,0)$ is given by:[26]

$$u(r,0) = 4\left(\frac{1-\nu^2}{\pi E_S}\right)\int \frac{\rho}{\rho+r} K\left[\frac{4r\rho}{(r+\rho)^2}\right] p(\rho)d\rho \quad (6)$$

where ν is the Poisson's ratio of the substrate, E_S is the Young's modulus of the substrate, K is the complete elliptic integral of the first kind, p is the pressure. In this case, the force found by integrating Eq. 5 will replace Eq. 3. It should be noted that Eq. 5 and Eq. 6 are coupled, and the instantaneous equilibrium surface profile must be calculated at each step in the simulation, outlined in §3.1.

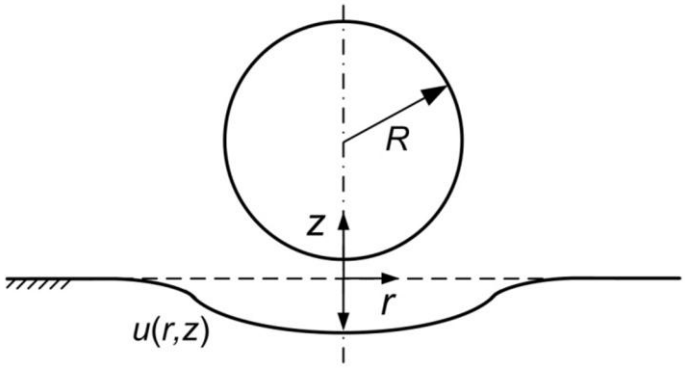

Fig. 2 System geometry under consideration, showing the deformation of the substrate surface due to elastohydrodynamic lubrication during the tip approach

2.4 Force applied to beam due to fluid squeezing, F_{SB}

The fluid is not only constrained between the tip and substrate, but also between the beam and substrate. The effect of squeeze flow damping on the cantilever beam presents a complex challenge because defining the cantilever shape is non-trivial when compared with that of a sphere or cone apex. This is because the cantilever beam is compliant and therefore its shape depends on the air pressure acting on it. The full solution to this problem requires computationally expensive numerics and does not lend itself to be used in a model such as this. However, Darling *et al*.[27] suggested a useful method of approximation. Reynolds lubrication equation describing squeeze flow is given as:

$$\nabla \cdot \left(\frac{D^3}{12\mu_{EFF}} p^{1/\eta} \nabla p\right) = \frac{\partial}{\partial t}\left(D p^{1/\eta}\right) \tag{7}$$

where t is time. As this is an isothermal process, in that the surfaces can be taken to be thermally conductive, η is assumed to be 1. For small variations in the local pressure and the gap where $p = P_a + \delta p$ and $D = D_0 + \delta D$, the Reynolds lubrication equation can be linearised into the form:

$$\nabla^2 P - \alpha^2 \frac{\partial P}{\partial t} = \alpha^2 \frac{\partial H}{\partial t} \tag{8}$$

Here $P = \delta p / P_A$ is the normalised local pressure variation, P_A is the ambient pressure, $H = \delta D / D_0$ is the normalised local gap variation, D_0 is the average instantaneous separation distance, and $\alpha^2 = \frac{12\mu_{EFF}}{{D_0}^2 P_A}$ is a constant. This equation has the form of a linear diffusion equation with a source term $\alpha^2 \frac{\partial H}{\partial t}$ which can be solved using a Green's function method.[28]

Diffusion from a point source excitation is described by:

$$\nabla^2 G - \alpha^2 \frac{\partial G}{\partial t} = -4\pi\delta(\boldsymbol{r} - \boldsymbol{r}_0)\delta(t - t_0) \tag{9}$$

Where $G(\boldsymbol{r}, t|\boldsymbol{r}_0, t_0)$ is the Green's function which represents the response at an observation point ($\boldsymbol{r}$,t) caused by an excitation at the source point $(\boldsymbol{r}_0, t_0)$**,** where t is time and t_0 is the initial time. For an arbitrary source term:

$${\nabla_0}^2 P - \alpha^2 \frac{\partial P}{\partial t_0} = -4\pi\rho_F(\boldsymbol{r}_0, t_0) = \alpha^2 \frac{\partial H}{\partial t_0} \tag{10}$$

the solution is expressible as an integral of the Green's function over the source points:

$$P(\boldsymbol{r},t) = \int_0^t \int_{V_0} G(\boldsymbol{r},t|\boldsymbol{r}_0,t_0)\rho_F(\boldsymbol{r}_0,t_0)d\boldsymbol{r}_0 dt_0 \quad (11)$$

where V_0 is the initial volume and ρ_F is the fluid density. The proper Green's function can be constructed as an expansion over the domain of the compressed volume. Assuming that the pressure variation is approximately constant in the direction of compression, the eigenfunctions u_{mn} and eigenvalues k_{mn} are solutions to a two-dimensional scalar Helmholtz equation:[29]

$$\nabla^2 u_{mn} + k_{mn}^2 u_{mn} = 0 \quad (12)$$

With nondegenerate eigenvalues, the eigenfunctions form a complete orthonormal set of expansion functions:

$$\int_{V_0} {u_{mn}}^*(\boldsymbol{r}) u_{m'n'}(\boldsymbol{r})d\boldsymbol{r} = \delta_{mm'}\delta_{nn'} \quad (13)$$

$$\sum_{m,n} u_{mn}(\boldsymbol{r}){u_{mn}}^*(\boldsymbol{r}_0) = \delta(\boldsymbol{r}-\boldsymbol{r}_0) \quad (14)$$

The Green's function is constructed from these expansion functions with time-varying coefficients:

$$G(\boldsymbol{r},t|\boldsymbol{r}_0,t_0) = \frac{4\pi}{\alpha^2}\Theta(t-t_0)\sum_{m,n} exp\left(\frac{-k_{mn}^2(t-t_0)}{\alpha^2}\right) u_{mn}(\boldsymbol{r}){u_{mn}}^*(\boldsymbol{r}_0) \quad (15)$$

Here $\Theta(t)$ is the unit step function.[29] Therefore, in order to calculate the force on the cantilever due to squeeze flow the correct eigenvalues and eigenfunctions and the corresponding Green's function need to be found. The solution is given when the pressure profile as given in Eq. 11 is integrated over the area of the cantilever.

For a rectangular AFM cantilever with dimensions according to the schematic shown in Fig. 1(b), the fluid gap is taken to occupy the domain $0 < x < L - dL$ and $0 < y < w$, where L is the beam length, w is the beam width and dL is the distance from the end of the beam to the position of the sphere or cone tip. The AFM cantilever is generally fixed from above, i.e. the fixed end is further from the flat surface than is the free end, and hence fluid is free to flow past the fixed end of the cantilever. Therefore the boundary condition at this location for Eq. 12 is $P = 0$. The same condition applies to the two vertical sides along the cantilevers length. At the location of the sphere or cone tip, it is assumed that air is prevented from flowing past, giving a boundary condition of $dP/dx = 0$ at $x = L - dL$.

Eq. 12 can be solved by using separation of variables. Applying the boundary conditions listed above gives the eigenfunctions as:

$$u_{mn}(x,y) = \sqrt{\frac{4}{w(L-dL)}}\sin\left(\frac{m\pi x}{2(L-dL)}\right)\sin\left(\frac{n\pi y}{w}\right) \quad (16)$$

With m = 1,3,5… and n = 1,2,3…. The corresponding eigenvalues are:

$$k_{mn}^2 = \left(\frac{m\pi}{2(L-dL)}\right)^2 + \left(\frac{n\pi}{w}\right)^2 \quad (17)$$

The deflection, δ, of a cantilever with a point load, F', acting normal to the deflected, tilted beam at a distance $L - dL$ from the fixed end can be calculated using:

$$\delta(x) = \frac{F'x^2}{6EI}[3(L-dL) - x] \quad (18)$$

The gap between the substrate and the cantilever has been amended to include the fact that the cantilever fixed end is tilted from the horizontal by angle θ, typically on the order 10 °, due to the way in which it is housed in the AFM instrument. Hence the normalized displacement of the cantilever relative to the substrate is given by:

$$H(x,y,t) = \frac{\dot{D}_{FIXED}}{D_0}t - \left(\frac{x}{L-dL}\right)\sin\theta\,\frac{\dot{D}_{FIXED}}{D_0}t - \left(\frac{\delta(x)}{L-dL}\right)\frac{(\dot{D}_T-\dot{D}_{FIXED})}{D_0}t \quad (19)$$

where $\dot{D}_{FIXED}$ is the drive velocity of the fixed end of the beam. The source term in Eq. 10 is then:

$$\rho(\boldsymbol{r}_0,t_0) = -\frac{\alpha^2}{4\pi}\frac{\partial H}{\partial t_0} = -\frac{\alpha^2}{4\pi}\left(\frac{\dot{D}_{FIXED}}{D_0} - \left(\frac{x}{L-dL}\right)\sin\theta\,\frac{\dot{D}_{FIXED}}{D_0} - \left(\frac{\delta(x)}{L-dL}\right)\frac{(\dot{D}_T-\dot{D}_{FIXED})}{D_0}\right) \quad (20)$$

The pressure term defined in Eq. 11 can therefore be shown to be:

$$P = \sum_m\sum_n \frac{32}{m^2n\pi^2}\sin\left(\frac{m\pi x}{2(L-dL)}\right)\sin\left(\frac{n\pi y}{w}\right)\left(\frac{\alpha^2}{k_{mn}^2}\right)\left[1-e^{-\frac{k_{mn}^2}{\alpha^2}t}\right]\left[\frac{F'(L-dL)^2}{EI}\frac{(\dot{D}_T-\dot{D}_{FIXED})}{D_0}\left(3(-1)^{\frac{m+1}{2}}+\frac{4}{m\pi}+\right.\right.$$
$$\left.\left.8m2\pi2-1m+12+DFIXEDD0m\pi-2\sin\theta-1m+12\right.\right. \quad (21)$$

Upon integrating the pressure over the cantilever surface, the expression for the force due to fluid squeezing is given by:

$$F_{SB} = -P_a\sum_m\sum_n\left\{\frac{384}{m^4n^2\pi^5}\left(\frac{\alpha^2}{k_{mn}^2}\right)\left[1-e^{-\frac{k_{mn}^2}{\alpha^2}t}\right]\left[\frac{F'(L-dL)^2}{EI}\frac{(\dot{D}_T-\dot{D}_{FIXED})}{D_0}\left(3(-1)^{\frac{m+1}{2}}+\frac{4}{m\pi}+\frac{8}{m^2\pi^2}(-1)^{\frac{m+1}{2}}\right)+\right.\right.$$
$$\left.\left.DFIXEDD0m\pi-2\sin\theta-1m+12-1m+12+4m\pi+8m2\pi2-1m+12\right.\right. \quad (22)$$

The negative sign in the first term in Eq. 22 shows that the force acts in the opposite direction to the direction of cantilever motion. The exponential term can be ignored in most situations as this term takes into account the initial effects caused by the sudden starting of the cantilever. For AFM cantilevers under normal conditions the exponent is very large and so these effects dissipate very quickly.

2.5 Weight of the tip, F_{WT}

The force due to the weight of the tip will act on the centre of mass of the tip, and hence the tip volume needs to be calculated, which is trivial for a sphere, and as such is suitable for a spherical colloid probe cantilever. However, AFM cantilever tips tend to be pyramidal in shape, with a hemispherical apex. The geometry considered is shown in Fig. 1(a), in which the tip is considered to be a blunt four-sided pyramid with hemispherical cap. Therefore, there are two separate expressions for the weight of the tip; one for a spherical colloid probe, F_{WTS}, and one for a pyramidal tip, F_{WTP}.

$$F_{WTS} = \frac{4}{3}\rho_T g\pi R^3 \quad (23)$$

$$F_{WTP} = \frac{\rho_T g}{3}[s^2(h_2-h_1) + 2\pi R^3] \quad (24)$$

where ρ_T is the density of the tip, g is the acceleration due to gravity, R is the radius of the spherical colloid probe or hemispherical tip apex of a pyramidal tip as shown in Fig. 1(a), s is the pyramid base length, h_2 is the height of the pyramid to its apex, and h_1 is the height of the pyramid to its blunt end in order to incorporate the terminal hemisphere.

2.6 Acceleration of the tip, F_{IT}

Similarly, as the sphere is in general moving at a different velocity to the fixed end velocity, it must at some point be accelerating, and the force will act on the centre of mass of the tip, which is also described by two separate expressions, depending on the choice of tip; one for a spherical colloid probe, F_{ITS}, and one for a pyramidal tip, F_{ITP}.

$$F_{ITS} = \frac{4}{3}\rho_T a_T \pi R^3 \tag{25}$$

$$F_{ITP} = \frac{\rho_T a_T}{3}[s^2(h_2 - h_1) + 2\pi R^3] \tag{26}$$

where a_T is the acceleration of the tip not due to gravity.

2.7 Weight of the beam, F_{WB}

The cantilever will exhibit a static deflection, $b(x)$, as a function of its length due to its own weight, which can be expressed as:

$$b(x) = \rho_B g \tau w \cos(\theta) \frac{x^2}{E_B I}\left(-\frac{x^2}{24} + \frac{xL}{6} - \frac{L^2}{4}\right) \tag{27}$$

where, ρ_B is the beam density, τ is the beam thickness, w is the beam width, E_B is the Young's modulus of the beam material, and I is the moment of inertia of the beam. The equivalent force can be found by considering the deflection of a cantilever with a force acting on its tip as given by:

$$b(x) = \frac{F_{WB}}{E_B I}\left(-\frac{\langle x-(L-dL)\rangle^3}{6} + \frac{x^3}{6} + \frac{(\langle x-(L-dL)\rangle - L)x^2}{2}\right) \tag{28}$$

Equating Eq. 27 and Eq. 28 and rearranging for the weight of the beam gives the equivalent force as:

$$F_{WB} = \frac{3W}{4\left(2+\frac{dL}{L}\right)} + \frac{WdL}{4L} \tag{29}$$

where $W = \rho_B g \tau w L \cos(\theta)$ and is the total weight taking into account the beam tilt angle.

2.8 Beam inertia, F_{IB}

Dealing with the effect of the acceleration of the tip is difficult because we do not know the shape of the beam and hence the acceleration distribution along its length. To give some estimate of the effect it will be assumed that the acceleration varies linearly along the beam with the maximum being the tip acceleration at the free end and zero at the fixed end which is of course travelling at the fixed velocity $\dot{D}_{FIXED}$. The deflection of a cantilever under such conditions can be shown to be:

$$b(x) = \rho_B a_T \tau w \cos(\theta) \frac{11x^5}{120 E_B I L} \tag{30}$$

Equating to Eq. 28 gives the equivalent force acting on the tip:

$$F_{IB} = \frac{-11\rho_B a_T \tau w L \cos(\theta)\left(\frac{dL}{L}-1\right)^3}{20\left(2+\frac{dL}{L}\right)} \tag{31}$$

Fig. 3 shows the comparison between the exact beam shape, as calculated from the Euler-Bernoulli beam equation, and the point load approximation. The line represents the exact shape of the cantilever due to distributed loads described by Eqs. 21, 27 and 30. The star indicates the deflection at the position of a pyramidal or spherical tip due to the equivalent point loads given by Eqs. 22, 29 and 31. The good agreement between the position of the star and the beam shape shows that the point load approximation is a valid assumption.

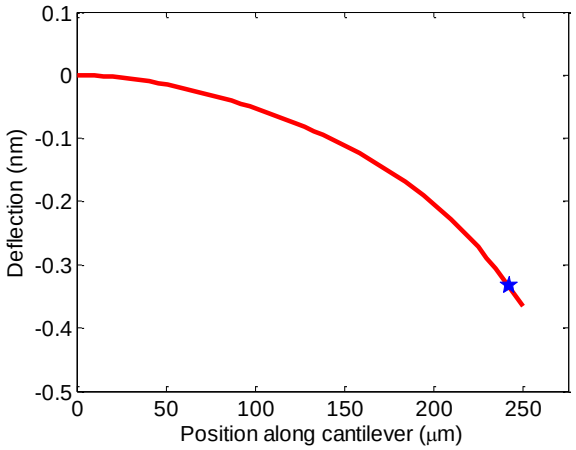

Fig. 3 Comparison between exact beam shape analysis (Eqs. 21, 27 and 30) and point load approximation (Eqs. 22, 29 and 31). It is assumed that the sphere is accelerating downwards at a rate $a_T = 10$ m/s^2, through air of viscosity μ =18.3 μPa.s (25 °C, 1 atm), $\dot{D}_{FIXED} = 100$ nm/s, $D_0 = 64.1$ μm, $R = 8.2$ μm, $\theta = 11$ °, and $\rho_B = 2330$ kg/m^3.

2.9 The dynamics of the cantilever

The motion of the cantilever as a function of time can now be described in terms of a second order differential equation:

$$m_{EFF}\frac{d^2\Upsilon}{dt^2} = k\left[\left(H_0 - \dot{D}_{FIXED}t\right) - \Upsilon\right] - F_V + F_{ST} - F_{WT} + F_{SB} + F_{IT} - F_{WB} + F_{IB} \qquad (32)$$

where k is the beam spring constant, H_0 is the initial tip position, Υ is the instantaneous position of the tip, and m_{EFF} is the effective mass of the tip and cantilever assembly. The second term, on the right hand side of Eq. 32, comes from equating the effective deflection due to a point load on the tip to the deflection due to the weight of the beam. Eq. 32 is the equation solved in order to elucidate the beam dynamics during the approach of the tip to a countersurface.

m_{EFF} for a pyramidal tip is given by m_{EFFP}:

$$m_{EFFP} = \frac{\rho_T}{3}[s^2(h_2 - h_1) + 2\pi R^3] + \frac{3\rho_B\tau wL}{8} \qquad (33)$$

m_{EFF} for a spherical colloid probe tip is given by m_{EFFS}:

$$m_{EFFS} = \frac{4}{3}\rho_T\pi R^3 + \frac{3\rho_B\tau wL}{8} \qquad (34)$$

2.10 The beam spring constant

The spring constant, or stiffness, of a beam with a point load acting normal to the cantilever at the point where the tip is attached can be shown to be (using Eq. 28):

$$k = \frac{3E_B I}{(L-dL)^3} \tag{35}$$

However because of the wide array of forces acting on different locations on the cantilever, the stiffness needs to be modified to take into account these forces and the torques they produce. One effect that needs to be accounted for is that Eq. 35 assumes that all the forces are acting normal to the neutral axis of the cantilever. This assumption is reasonable if the cantilever is not tilted and the deflections are very small, i.e. if the angle of the tip tends to zero. For the case considered here, the fixed end of the cantilever is tilted initially to a pre-determined angle, θ, typically 10-12 ^{o} from the horizontal, while all the forces act vertically. This can be accounted for by resolving the forces in the normal direction. The forces in the axial direction will generally be small in comparison to forces in the horizontal and normal directions, and therefore can be assumed to have a negligible effect on the stiffness of the cantilever. Eq. 35 also assumes that the forces are acting directly on the neutral axis of the cantilever.

As was shown by Edwards *et al*.,[30] when a beam has a feature at its free end, such as a colloid probe or a pyramidal tip, the forces acting either on the probe cause an additional bending moment to act on the beam, owing to the distance the force now acts from the neutral axis. This extra torque affects the cantilever shape and therefore the direction the forces are acting relative to the orientation of the cantilever, thus changing its stiffness. Fig. 4 shows an example geometry and angle convention for a colloid probe cantilever, from which the forces acting upon the tip are defined.

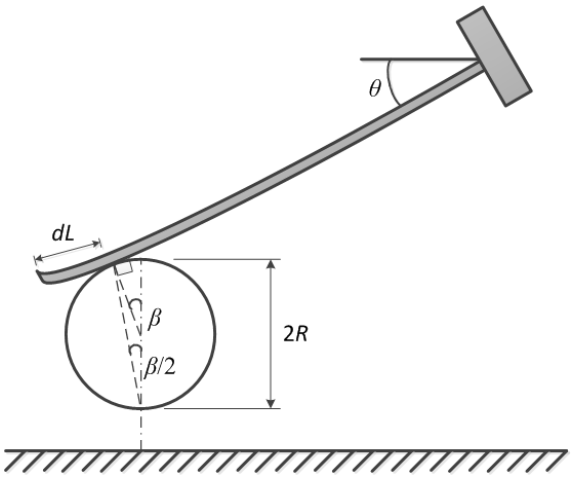

Fig. 4 Cantilever geometry and angle convention for forces acting upon the tip

Edwards *et al*.[30] expressed the normal force and the torque in terms of the applied force normal to the substrate, and the applied force perpendicular to the free end of the cantilever. Here we define the torque, T, the applied force normal to the substrate, F, and the applied force perpendicular to the free end of the cantilever, F'. The resultant equations are therefore:

$$F' = F\cos\theta \tag{36}$$

$$T = -FJ\sin\alpha \tag{37}$$

Here J is the distance between the point of application of the force and the neutral axis and α is the angle of the force with respect to the cantilever normal. However these relationships are only true for an undeflected

cantilever. When a force is applied to the cantilever, it will deflect causing the angle associated with the force to change correspondingly. Therefore the actual torques and normal forces are instead described as:

$$F' = F\cos\beta \tag{38}$$

$$T = -FJ\sin\beta \tag{39}$$

where β is the equilibrium angle between the axis perpendicular to the free end of the cantilever and the axis normal to the surface. Therefore to calculate the stiffness, it is necessary to find the torques, normal forces and the angle of the tip associated with all the forces that have been applied to the cantilever. Only the forces acting on the tip will induce a torque, and these forces can be split into (i) the forces acting on the centre of the tip, which are the tip weight, tip inertia, and the van der Waals force; and (ii) the squeeze flow force acting on the bottom of the tip. The torque associated with the forces listed under (i) take the form:

$$T_{CEN} = -FR\sin\beta \tag{40}$$

The torque associated with the squeeze flow, (ii), take the form:

$$T_{SQ} = -2FR\cos(\beta/2)\sin\beta \tag{41}$$

The total torque can therefore be shown to be:

$$T_{TOTAL} = -F'_V R\sin\beta + 2F'_{ST}R\cos(\beta/2)\sin\beta - F'_{WB}R\sin\beta + F'_{IT}R\sin\beta \tag{42}$$

The dashes denote that it is the forces perpendicular to the free end of the cantilever beam that are being considered as defined in Eq. 38. The angle of the tip under the influence of the various torques and forces can be shown to be:

$$\beta = \theta + \tan^{-1}\left(\begin{matrix}\frac{T_{TOTAL}(L-dL)}{E_B I} - \left(\frac{(F'_V - F'_{ST} - F'_{SB} + F'_{WT} - F'_{IT})(L-dL)^2}{2EI}\right) \\ -\frac{\rho_B g t w\cos(\beta)L^3}{6E_B I} + \frac{\rho_B a_T t w\cos(\beta)L^3}{8E_B I}\end{matrix}\right) \tag{43}$$

The terms inside the inverse tangent function are, in order from left to right, (i) the gradient due to the torque, (ii) the gradient due to the forces on the sphere, (iii) the gradient due to the weight of the cantilever, and (iv) the gradient due to the cantilever's inertia. In order to find the equilibrium angle β and hence the correct forces, Eqs. 40 and 41 need to be solved iteratively by first assuming $\beta = \theta$ and iterating until convergence. Once this has been achieved, the stiffness can be calculated simply by dividing the applied force by the deflection thus:

$$k = \frac{F_V - F_{ST} - F_{SB} + F_{WT} - F_{IT} + F_{WB} - F_{IB}}{\frac{T_{TOTAL}(L-dL)^2}{2E_B I} - \left(\frac{(F'_V - F'_{ST} - F'_{SB} + F'_{WT} - F'_{IT})(L-dL)^3}{3E_B I}\right) - \frac{\rho_B g\tau w\cos(\beta)L^4}{8E_B I} + \frac{11\rho_B a_T \tau w\cos(\beta)L^4}{120E_B I}} \tag{44}$$

3. Experimental details

3.1 Jump-to simulations

The time-dependent motion of the cantilever is described by a second order differential equation (Eq. 30), which was solved numerically using a built-in stiff solver, ODE15s, from the MatLab ODE suite (MatLab 7.0.1, MathWorks Inc., USA). It is a multi-step, variable order solver based on the numerical differentiation formulas.[31] The absolute tolerance and hence the threshold below which the value of the i^{th} solution component was set was 10^{-18}, which corresponds to an accuracy of 10^{-16}. The computation procedure is shown as a flowchart in Fig. 5.

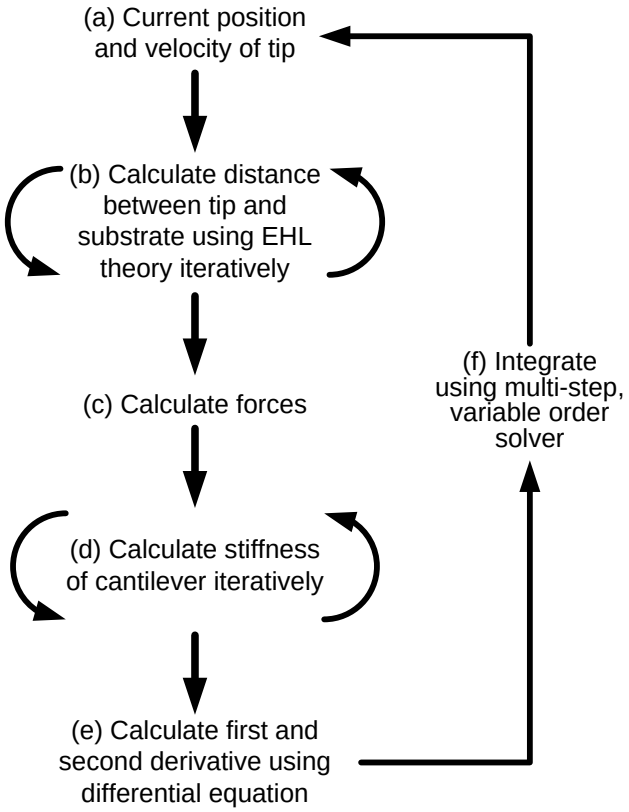

Fig. 5 Flowchart describing the calculation of the cantilever motion

In step (a), it is assumed the current tip position and velocity are known whether they were calculated from the previous step in the simulation or defined from the initial conditions. These conditions assume that the AFM cantilever approaches the surface from a long distance away (*c.a.* 1 mm) so that it was initially unaffected by van der Waals forces and hence undeflected. Therefore the initial tip position is 1 mm and the initial velocity is equal to the specified fixed end velocity.

The tip position and velocity is then used in Eqs. 5 and 6 to calculate the hydrodynamic force, the deflection of the substrate and hence the gap. As discussed in §2.3, this is done iteratively in step (b). In step (c), these data are used in Eqs. 1, 20, 21, 22, 23, 24, 27, 29 to calculate the various forces acting on the cantilever. The forces are combined in step (d) to calculate the resultant force and torque acting on the cantilever and hence find its effective stiffness. These forces are resolved in step (e) using Newton's second law to form the differential equation that defines the motion of the cantilever. This is numerically integrated using the method discussed to calculate the instantaneous tip position and velocity which then feeds into step (a).

3.2 Hamaker constants

Hamaker constants for the tip/air/substrate interaction were calculated using Eq. 45,[21] where 1 denotes the tip, 2 denotes the substrate, 3 denotes the air, ε_i is the static dielectric constant of material i, n_i is the refractive index of material i, k_B is Boltzmann's constant, T is the temperature, h is Planck's constant, and v_e is the plasma frequency of the free electron gas, which is typically in the range 3-5×10^{15} s^{-1}, and therefore provides upper and lower bounds to the value of the Hamaker constant.

$$A = \frac{3k_B\mathrm{T}}{4}\left(\frac{\varepsilon_1-\varepsilon_3}{\varepsilon_1+\varepsilon_3}\right)\left(\frac{\varepsilon_2-\varepsilon_3}{\varepsilon_2+\varepsilon_3}\right) + \frac{3hv_e}{8\sqrt{2}}\frac{(n_1^2-n_3^2)(n_2^2-n_3^2)}{(n_1^2+n_3^2)^{0.5}(n_2^2+n_3^2)^{0.5}\left[(n_1^2+n_3^2)^{0.5}+(n_2^2+n_3^2)^{0.5}\right]} \quad (45)$$

3.3 AFM measurements

AFM force measurements were performed using a NanoWizard II AFM (JPK, UK) operating in contact mode at a temperature of 18 °C and a relative humidity in the range 40-50 %. The AFM was seated on a Micro 40 active vibration isolation system (Accurion, Germany) and housed within an acoustic enclosure (JPK, UK) to minimise the effect of ambient noise. A rectangular Si cantilever with a pyramidal tip of 8 nm nominal tip radius (RTESP, Veeco, UK) and a rectangular Si cantilever modified at its apex with a 8.2 µm radius SiO_2 colloid probe (Novascan, USA) were employed for the force measurements. Pyramidal tip cantilevers were used as received and a new cantilever was used for each substrate measured. Their maximum tip radius as specified by the manufacturer was 12 nm. Cantilever spring constants were calibrated according to the method described by Bowen *et al*.[32] and were calculated to be (i) 39.9 ± 2.1 N/m for the pyramidal tip cantilever, and (ii) 4.1 ± 0.2 N/m for the colloid probe cantilever. Measurements were performed over the drive velocity range 10 nm/s to 100 µm/s, and data were acquired at a rate of 10 kHz throughout. 100 measurements were made for each drive velocity, spaced equally in a 10 x 10 grid array across a 100 µm x 100 µm area of the sample surface.

The substrates employed were 1 mm thickness glass microscope slides (BDH, UK), 3 mm thickness poly(propylene) slabs (in-house supply), and 3 mm thickness poly(dimethylsiloxane) slabs, prepared using Type 184 Sylgard mix (Dow Corning, USA) at a 5:1 w/w ratio of silicone to curing agent, with the curing step performed at 20 °C for a minimum of 7 days. Substrate surface roughnesses were evaluated via contact mode AFM imaging, employing a pyramidal-tipped Si_3N_4 AFM cantilever (DNP-S, Veeco, UK) with a nominal tip radius of 25 nm. The mean roughness (R_A) and peak-to-valley roughness (R_Z) of each substrate surface was calculated from an image of lateral dimensions 5 x 5 µm.

3.4 Nanoindentation

The hardness and reduced modulus of the glass, poly(propylene) and poly(dimethylsiloxane) were measured using a NanoTest nanoindenter (Micro Materials, UK) operating a diamond-coated Berkovich pyramidal indenter. Indentation depths were at least one order of magnitude greater than the R_A of the substrate surface. A minimum of 16 indents were performed for each material.

4. Results

4.1 Substrate properties

For the substrates employed in the work presented here, Table 1 lists the dielectric constant (ε), refractive index (n), Hamaker constant versus SiO_2 (A), hardness (H_S), Poisson's ratio (ν_S), reduced modulus ($E_S{}^*$), Young's modulus (E_S), mean surface roughness (R_A), peak-to-valley surface roughness (R_Z), and static water contact angle in air (Θ_W). Hamaker constants were calculated according to the method described in §3.2. Fig. 6 shows the surface topographies of the substrates as measured using AFM. The results show that the substrates can be listed in order of increasing Young's modulus as poly(dimethylsiloxane) < poly(propylene) < glass, with approximately two orders of magnitude difference in modulus between each substrate.

Table 1. Summary of substrate physical and mechanical properties

Property	**Glass**	**Poly(propylene)**	**Poly(dimethylsiloxane)**
ε	3.9	2.2	2.5
n	1.46	1.49	1.40
A vs $SiO_2 \times 10^{-19}$ (J)	2.813 - 4.682	2.862 - 4.766	2.696 - 4.488
H_S (MPa)	6,200 ± 200	21.4 ± 0.6	0.95 ± 0.28
ν_S	0.2	0.5	0.5
$E_S{}^*$ (MPa)	78,010 ± 635	634 ± 44	3.62 ± 0.39
E_S (MPa)	74,890 ± 609	476 ± 33	2.71 ± 0.29
R_A (nm)	0.28	30.9	1.91
R_Z (nm)	4.6	557	139
Θ_W (°)	0	76	98

(a) For calculation of A according to Eq. 45, $\varepsilon_{air} = 1.0059$ and $n_{air} = 1.0003$; values taken from the CRC Handbook of Chemistry and Physics 92nd Edition [33]

(b) Upper and lower bounds on the value of A are presented due to uncertainty in the value of the plasma frequency of the free electron gas, υ_e

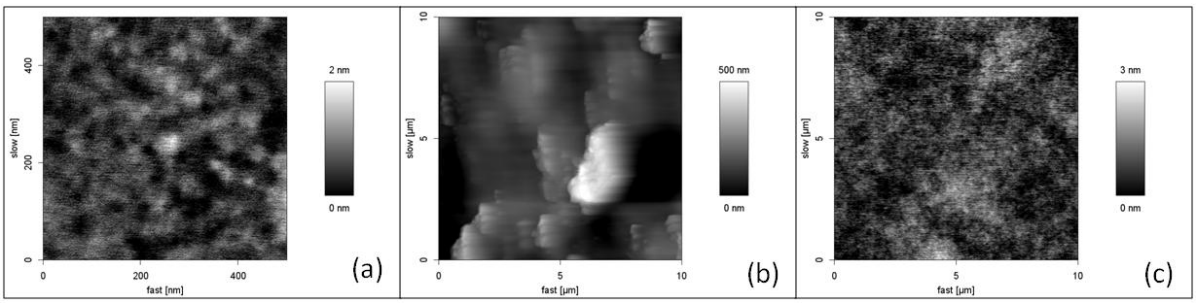

Fig. 6 Surface topographies of substrates measured using AFM; (a) glass, 500 x 500 x 2 nm; (b) poly(propylene), 10 x 10 x 0.5 µm; (c) poly(dimethylsiloxane), 10 x 10 x 0.003 µm.

4.2 Jump-to measurements and simulations

Fig. 7(a) is a schematic showing the position of the cantilever fixed end and free end as a function of time, as the cantilever fixed end is driven vertically downwards. Fig. 7(b) shows the resultant cantilever deflection as the free

end of the cantilever deflects increasingly downwards towards the substrate, until the tip makes contact with the surface. The deflection represented by distance C is the jump-to distance reported. For the simulated results, the criteria for deciding whether the tip was about to make contact with the substrate is as follows. The cantilever deflection was considered to be unstable if the tip velocity increased to a value greater than 5x the drive velocity. Choosing a velocity between 2x and 8x made no appreciable difference to the jump-to distance, owing to the very rapid increase in velocity at this point.

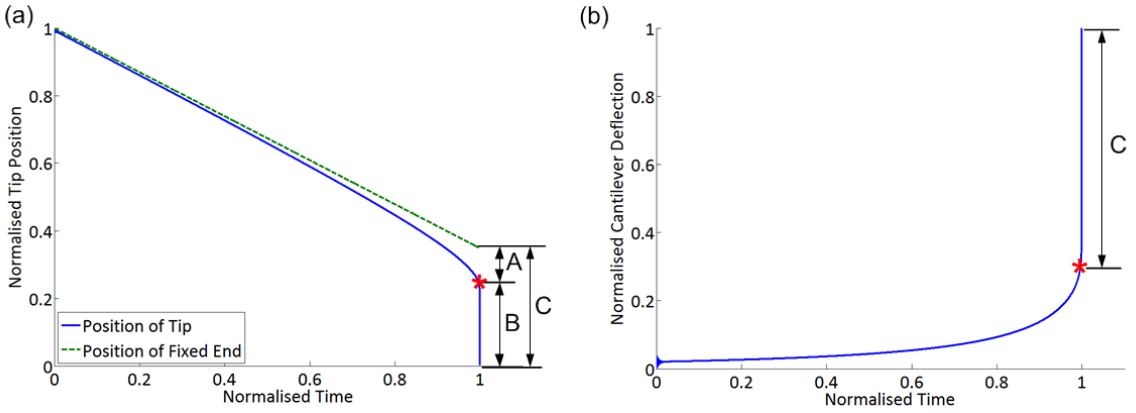

Fig. 7 Calculated fixed end motion, tip motion, and cantilever deflection, as a function of time; C denotes the jump-to distance

Fig. 8 shows the measured jump-to data at a drive velocity of 1 µm/s for glass, poly(propylene) and poly(dimethylsiloxane) versus (a) pyramidal tips and (b) spherical colloid probes. The figures show the displacement of the cantilever free end as the fixed end is approached towards the sample surface. For pyramidal tip cantilevers, the glass/pyramid system exhibits the largest jump-to distance of approximately 1 nm. The poly(propylene)/pyramid and poly(dimethylsiloxane) pyramid systems both exhibit jump-to distances of < 1 nm. For spherical colloid probes, the jump-to distance for the glass/sphere and poly(propylene)/sphere systems are 5.7 nm and 7.2 nm respectively. However, the jump-to distance for the poly(dimethylsiloxane)/sphere system is 195 nm.

There is evidence of weak electrostatic attraction for the poly(propylene)/sphere system, which can be seen as a long-range deflection of the cantilever, even though the sphere is out of contact with the substrate. The deflection increases as the sphere approaches the surface, and over the 450 nm fixed end distance of the data shown in Fig. 8(b), there is a vertical deflection of 5 nm before the jump-to instability. No electrostatic effect is visible for the glass/sphere or poly(dimethylsiloxane)/sphere systems, nor for any of the pyramidal tip systems. The jump-to distances reported for the poly(propylene)/sphere system do not include the additional vertical deflection imparted on the beam due to electrostatic attraction.

The gradient of the deflection/displacement data in the region where the tip is in contact with the surface provides information regarding the mechanical properties of the substrate. For both pyramidal tips and spherical colloid probes, poly(dimethylsiloxane) exhibits a greater compliance than glass and poly(propylene), which is in agreement with the values of Young's modulus listed in Table 1, whereby poly(dimethylsiloxane) has the lowest Young's modulus of the three substrates.

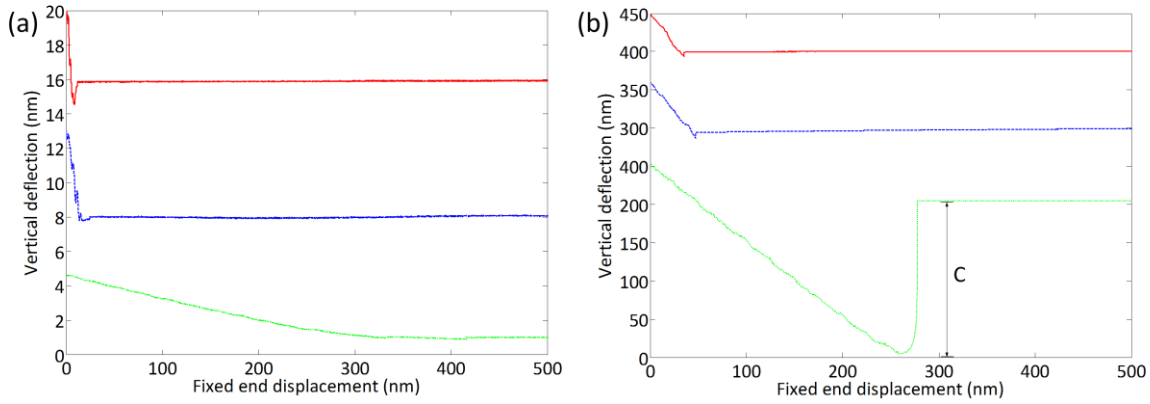

Fig. 8 Measured AFM jump-to data at 1 μm/s drive velocity for (a) pyramidal tips versus glass (continuous line), poly(propylene) (dashed line), poly(dimethylsiloxane) (dotted line), and (b) spherical colloid probes versus glass (continuous line), poly(propylene) (dashed line), poly(dimethylsiloxane) (dotted line); C denotes the jump-to distance.

Fig. 9 shows the comparison between the jump-to distances measured using AFM and the jump-to distances calculated using the simulation procedure outlined in §3.1. Upper and lower bounds for the simulated jump-to distance are presented due to the upper and lower bounds placed on the calculated value of A. The results obtained using (i) pyramidal tips and (ii) spherical colloid probes are described in §4.2.1 and §4.2.2.

4.2.1 Pyramidal tips

Fig. 9(a) shows that there is reasonable order-of-magnitude agreement between measurement and simulation for the glass/pyramid system, although the theory systematically underestimates the jump-to distance. Fig. 9(b) shows good agreement between measurement and simulation for the poly(propylene)/pyramid system, and Fig. 9(c) shows reasonable order-of-magnitude agreement between measurement and simulation, although in this case the theory systematically overestimates the jump-to distance. For all three cases, jump-to distances are of the order 0.1-1 nm, and in all three cases there is a decrease in the jump-to distance for drive velocities greater than 10 μm/s, a feature present in both the simulated and measured results. The decrease in measured jump-to distance at large drive velocities is most pronounced for the glass/pyramid system. For the simulated results, there is approximately a 24 % decrease in the jump-to distance over the drive velocity range investigated.

4.2.2 Spherical colloid probes

Figs. 9(d) and 9(e) show that there is reasonable order-of-magnitude agreement between measurement and simulation for the glass/sphere and poly(propylene)/sphere systems, with jump-to distances in the range 1-12 nm, whereas the simulated jump-to distances are in the range 4-5 nm. The measurement results exhibit a pronounced velocity dependence whereby jump-to distances decrease with increasing drive velocity. This feature is present in the simulation results, but is not as pronounced as in the measured results, nor is it as apparent as for those measurements and simulations performed using cantilevers presenting pyramidal tips. There is approximately a 5 % decrease in the simulated jump-to distance over the drive velocity range investigated. Fig. 9(f) shows that there is a pronounced deviation between measurement and simulation for the

poly(dimethylsiloxane)/sphere system, with measured jump-to distances in the range 100-250 nm, whereas the simulated jump-to distances are in the range 4-5 nm.

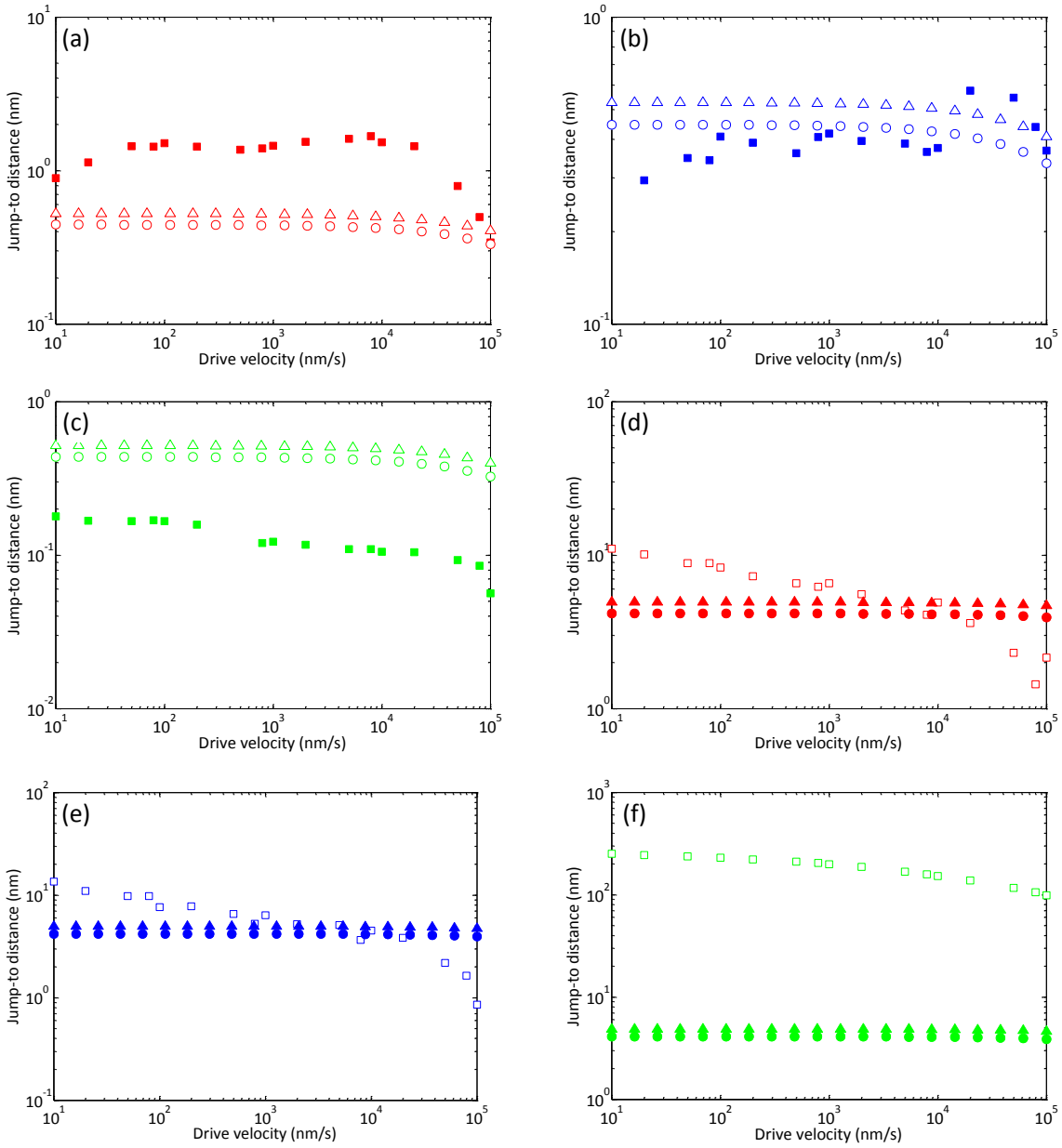

Fig. 9 Measured (□) and simulated (upper bound Δ, lower bound ○) jump-to distances for (a) glass/pyramid, (b) poly(propylene)/pyramid, (c) poly(dimethylsiloxane)/pyramid, (d) glass/sphere, (e) poly(propylene)/sphere, (f) poly(dimethylsiloxane)/sphere.

5. Discussion

5.1 Comparison between measurement and simulation

Comparison of the results for a cantilever presenting a pyramidal tip reveals that there is approximate agreement in the jump-to distance for glass, poly(propylene) and poly(dimethylsiloxane). For all three substrates, the jump-to distances are in the range 0.1-1 nm. The discrepancy between the measured distances and the simulated distances cannot currently be explained. However, it is interesting to note that the poly(dimethylsiloxane)/pyramid system displays the greatest discrepancy, whereby measured distances smaller than the simulated distances were recorded. The mechanism underlying this trend is not fully understood.

Comparison of the results obtained for a cantilever presenting a spherical colloid probe reveals that for the glass/sphere and poly(propylene)/sphere systems there is good approximate agreement between the measured and simulated jump-to distances. For the poly(dimethylsiloxane)/sphere system, the measured jump-to distances are two orders of magnitude greater than for the simulated jump-to distances. The Young's modulus of poly(dimethylsiloxane) is significantly lower than poly(propylene) and glass, and it could be that the compliance of the surface is an important parameter. This is discussed further in §5.2.

Poly(propylene) exhibits the highest mean surface roughness (R_A) of 30.9 nm, which suggests that the discrepancy between measurement and simulation is not significantly influenced by surface topography, for the range of topographies on display in this work, as shown in Fig. 6. The theory outlined in §2 assumes that the substrate surface is planar and flat with respect to the approaching spherical tip. If surface roughness were the determining factor, one might reasonably expect poly(propylene) to exhibit the greatest discrepancy between measurement and simulation. As it is, poly(dimethylsiloxane) exhibits the greatest discrepancy. Furthermore, it is anticipated that such an effect would only become important for spherical colloid probe tips, where the tip radius is much larger than the surface roughness. For pyramidal tips, the topography of the surface local to the 10 nm radius tip should always be effectively planar in comparison.

Interestingly, all of the measurements display a velocity dependence on the jump-to distance. This dependence generally covers the entire drive velocity range investigated, rather than just drive velocities greater than 1 μm/s, which is the suggested range of the effect for the simulated results. The velocity dependence occurs due to the viscous and inertial forces acting on the beam and probe resulting in a finite time required for the cantilever to deflect downwards in response to the attractive interactive forces. At high velocities, this finite time becomes comparable to the velocity with which the fixed end is approaching the substrate, and hence the jump-to distance is decreased. The velocity dependence is more pronounced for the sphere systems measured than for the pyramid systems. The simulations show that the dominant forces acting on the AFM are the van der Waals forces, squeeze flow at the tip, and also tip and beam inertia. For the range of experiments shown the simulations also show that the torque can increase the stiffness of the cantilever by up to 10 %.

5.2 Effect of substrate compliance

The numerical simulations show that EHL does not account for the effect the substrate compliance has on the larger-than-expected jump-to distance. This is because as the tip gets very close to the substrate, the air pressure slows down the tip velocity considerably. This in turn causes the pressure and hence substrate deflection to also decrease. This process means when the tip finally makes contact, its velocity is very low, despite its initial high

velocity just after the instability, and the deflection of the substrate is negligible, hence not contributing to the jump-to distance.

Parker and Attard[15] considered the deformation of surfaces due to attractive surface forces such as van der Waals interactions, and reported that for a non-compliant system in which the separation distance between two spheres, of radius R, is decreased quasi-statically, the separation distance, c, at which the two surfaces jump into contact is given by Eq. 46:

$$c = \left(\sqrt{2R}\frac{3A}{8}\frac{1-\nu^2}{E_S}\right)^{\frac{2}{7}} \quad (46)$$

Although Eq. 46 is formulated for a sphere-on-sphere system, using the approximations $1/R^* = 1/R_1 + 1/R_2$ and $1/E^* = 1/E_1 + 1/E_2$, we can estimate the equivalent separation distance for a sphere-on-flat system and for two dissimilar materials. Hence, using the values of A, E_S and ν given in Table 1, taking the value of R to be 12 nm for the pyramidal tip systems, and 8.2 μm for the spherical colloid probe systems, Eq. 46 provided approximate agreement with the measured and simulated values of the jump-to distance reported in §4.2 for the glass/pyramid and poly(propylene)/pyramid systems. However, Eq. 46 provided poor agreement for the poly(dimethylsiloxane)/pyramid system and all three sphere systems. The measured and simulated jump-to distances used for comparison were those for a fixed end drive velocity of 20 nm/s. This result suggests that the compliance of the surface cannot be dealt with in a trivial fashion.

Table 2. Comparison of calculated (Eq. 46), measured and simulated jump-to distances

System	Measured (nm)	Simulated (nm)	Calculated (nm)
Glass/pyramid	1.1	0.5	0.3
Poly(propylene)/pyramid	0.3	0.5	1.1
Poly(dimethylsiloxane)/pyramid	0.2	0.5	4.7
Glass/sphere	10.1	4.9	0.7
Poly(propylene)/sphere	16.2	5.0	2.8
Poly(dimethylsiloxane)/sphere	243.5	4.9	12.4

Another potential cause of the compliance effect may be due to the substrate swelling, not sinking. Forcada *et al*.[34-35] reported on the apparent swelling of thin liquid films when attempting to measure their thicknesses using AFM, finding that as the AFM tip approached the liquid/air interface there appeared to be an instability in the film, induced by van der Waals interactions between the tip and film. The instability caused an upwards swelling of the film towards the AFM tip, and hence contact with the tip was made prematurely when compared to the unperturbed film neighbouring the swelling. Hence, the film thicknesses measured by AFM were systematically larger than those measured using ellipsometry, a non-contact technique and hence not subject to the swelling effect. It is proposed that a similar effect is occurring here for the measurements made using the spherical colloid probe tips, whereby there is an upwards deformation of the substrate surface due to van der Waals interactions, followed by a retreat of the deformation and downwards deformation below the initial unperturbed surface position, caused by elastohydrodynamic lubrication. Such an effect would give the impression that the AFM tip is jumping into contact from a greater separation distance than would be anticipated were the substrate surface not deformable, due to the fact that one monitors the deflection of the AFM cantilever tip, and cannot directly observe the position of the surface underneath the tip. Fig. 10 shows a schematic of this hypothesised process, whereby the substrate surface deflects upwards prior to contact, and is subsequently deflected downwards by elastohydrodynamic lubrication, before the tip finally makes contact with the substrate.

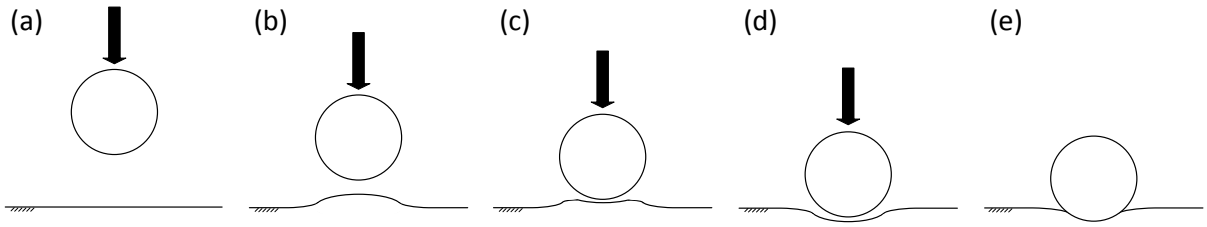

Fig. 10 Proposed schematic of surface deformation. (a) Tip approaches towards substrate surface. (b) Upwards substrate deformation due to van der Waals interactions. (c) Downwards substrate deformation due to elastohydrodynamic lubrication. (d) Increased downwards substrate deformation beyond initial unperturbed position. (e) Tip in contact with substrate under compressive normal load.

5.3 Additional contributory factors

Upon the approach of the pyramidal or spherical probe towards the substrate surface, it is possible that the presence of a thin liquid film, such as ubiquitous contamination or adsorbed water, or the existence of strong electrostatic interactions will affect the measured jump-to distance. However, both of these phenomena tend to be visible on the measured force-displacement data, examples of which are shown in Fig. 11. The approach of a spherical SiO_2 colloid probe towards a surface coated with a 0.1 Pa.s poly(dimethylsiloxane) liquid film of thickness 890 nm is shown in Fig. 11(a); details regarding film manufacture and characterisation have previously been described by Bowen *et al*.[36] Immediately after contact is made, it can be seen that the probe travels through the thickness of the film with the cantilever under tension, before the point of closest approach to the countersurface is reached, and the cantilever begins to bend upwards, until finally a compressive load is applied to the surface. The jump-to distance for this system is of the order 100 nm. The liquid surface is deformable

Fig. 11(b) shows the approach of a spherical SiO_2 colloid probe towards a poly(dimethylsiloxane) elastomeric surface which has recently undergone electron beam irradiation.[37] It can be seen that there is a long-range attractive deflection applied to the cantilever, which culminates in a deep curved descent of the probe towards the surface, over a fixed end displacement which is much greater than that over which a van der Waals-induced jump-to event takes place.

For the measurements presented in this work, there is no evidence of the presence of a thin liquid film. The relative humidity of the atmosphere in which the measurements were performed was in the range 40-50 %. Jones *et al*.[38] previously reported that for AFM measurements between hydrophilic surfaces, capillary contributions to pull-off forces become significant at a relative humidity of 60 % and above, due to liquid film formation. Hence, for the hydrophilic glass surface, and the hydrophobic poly(propylene) and poly(dimethylsiloxane) surfaces, it is not expected that a thin water film would form, nor does the jump-to data show any evidence of this phenomenon.

As mentioned in §4.2, there is a weak electrostatic attraction visible in the jump-to data for the poly(propylene)/sphere system, observable as a long-range deflection of the cantilever. However, this phenomenon is significantly less pronounced than the effect shown in Fig. 11(b), which shows data for a measurement performed using a SiO_2 colloid probe of similar diameter to that used for the jump-to measurements. None of the other sets of data presented here show any indication of electrostatic effects.

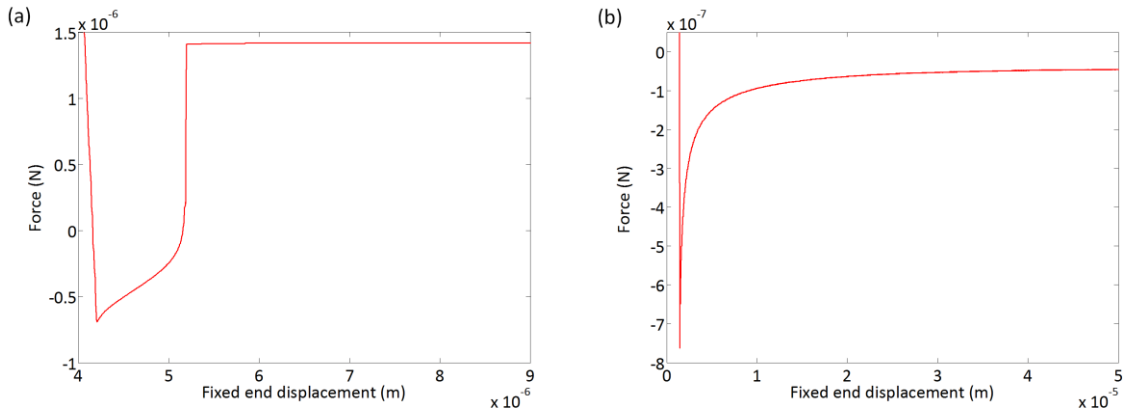

Fig. 11 Measured AFM jump-to data for a spherical colloid probe versus (a) 890 nm thickness poly(dimethylsiloxane) liquid film with 0.1 Pa.s viscosity, and (b) electron beam irradiated poly(dimethylsiloxane).

5.4 Future work

Considering only the experimental measurements for a moment, the large discrepancy in jump-to distances observed for the poly(dimethylsiloxane)/sphere system is interesting and worthy of further investigation. Further experimental work is required in order to assess the discrepancies reported here. Such investigations should extend to attempting measurements under vacuum conditions, in order to negate the possibility of elastohydrodynamic lubrication. Furthermore, it would be interesting to perform similar measurements using spherical colloid probes of varying modulus, against a substrate whose Young's modulus makes it effectively rigid in comparison. Such measurements would hopefully provide additional understanding as to whether the discrepancy in jump-to distance is due to a deformation of the more compliant material.

6. Conclusions

In this work a theoretical model of the dynamics of the approach of an AFM cantilever tip towards a surface was developed, which sought to capture the role played by the numerous forces involved during the van der Waals-induced jump-to phenomenon. A sphere-on-flat configuration was employed for the force balance, in which (i) a spherical colloid probe, and (ii) a pyramidal tip is attached near to the end of the approaching cantilever beam. The cantilever mechanics attempted to take into account the motion of the air through which the cantilever moves, the acceleration, inertia and torque of the cantilever, and the squeezing of the fluid between the sphere and the flat surface, leading to elastohydrodynamic lubrication and deformation of the substrate surface. Simulations of the cantilever approach towards (a) a glass substrate, (b) a poly(propylene) substrate and (c) a poly(dimethylsiloxane) substrate were performed, and AFM measurements were also made between the two types of tip and the three types of substrate, over a wide range of drive velocities.

The simulated jump-to distances were found to be in good approximate agreement with the experimental jump-to distances for systems involving a pyramidal tip, and also for the approach of a spherical colloid probe towards a glass substrate. However, for the approach of a spherical colloid probe towards poly(propylene) and poly(dimethylsiloxane) the experimental jump-to distances were one or two orders of magnitude greater than the simulated jump-to distances, an effect which is possibly due to a van der Waals-induced upwards deformation of the substrate surface towards the tip prior to contact, which would give the impression that the AFM tip is jumping into contact from a greater separation distance than would be anticipated were the substrate surface not deformable.

Acknowledgements

The authors gratefully acknowledge the assistance of Dr James Andrews for useful discussions throughout the preparation of this manuscript. The atomic force microscope and nanoindenter used in this research were obtained through Birmingham Science City: Innovative Uses for Advanced Materials in the Modern World (West Midlands Centre for Advanced Materials Project 2), with support from Advantage West Midlands (AWM) and part funded by the European Regional Development Fund (ERDF).

References

1. Binnig, G.; Quate, C. F.; Gerber, C. Atomic force microscope. *Phys. Rev. Lett.* **1986**, *56*, 930-933.
2. Ducker, W. A.; Senden, T. J.; Pashley, R. M. Direct measurement of colloidal forces using an atomic force microscope. *Nature* **1991**, *353*, 239-241.
3. Butt, H-J. Measuring electrostatic, van der Waals, and hydration forces in electrolyte solutions with an atomic force microscope. *Biophys. J.* **1991**, *60*, 777-785.
4. Weisenhorn, A. L.; Maivald, P.; Butt, H-J.; Hansma, P. K. Measuring adhesion, attraction, and repulsion between surfaces in liquids with an atomic force microscope. *Phys. Rev. B* **1992**, *45*, 11226-11232.
5. Fielden, M. L.; Hayes, R. A.; Ralston, J. Surface and capillary forces affecting air bubble-particle interactions in aqueous electrolyte. *Langmuir* **1996**, *12*, 3721-3727.
6. Preuss, M.; Butt, H-J. Direct measurement of particle-bubble interactions in aqueous electrolyte: Dependence on surfactant. *Langmuir* **1998**, *14*, 3164-3174.
7. Snyder, B. A.; Aston, D. A.; Berg, J. C. Particle-drop interactions examined with an atomic force microscope. *Langmuir* **1997**, *13*, 590-593.
8. Gady, B.; Schleef, D.; Reifenberger, R.; Rimai, D. S. The interaction between micrometer-size particles and flat substrates: A quantitative study of jump-to contact. *J. Adhesion* **1998**, *67*, 291-305.
9. Cappella, B.; Dietler, G. Force-distance curves by atomic force microscopy. *Surf. Sci. Rep.* **1999**, *34*, 1-109.
10. Attard, P.; Carambassis, A.; Rutland, M. W. Dynamic surface force measurement. 2. Friction and the atomic force microscope. *Langmuir* **1999**, *15*, 553-563.
11. Attard, P.; Gillies, G. Deformation and adhesion of viscoelastic particles: theory and experiment. *Aust. J. Chem.* **2001**, *54*, 477-485.
12. Butt, H-J.; Stark, R. Atomic force microscopy in structured liquids - remark on the interpretation of jumps in force curves. *Colloid. Surface. A* **2005**, *252*, 165-168.
13. Das, S.; Sreeram, P. A.; Raychaudhuri, A. K. A method to quantitatively evaluate the Hamaker constant using the jump-into-contact effect in atomic force microscopy. *Nanotechnology* **2007**, *18*, 035501.
14. Attard, P. Measurement and interpretation of elastic and viscoelastic properties with the atomic force microscope. *J. Phys. Condens. Matter* **2007**, *19*, 473201.
15. Parker, J. L.; Attard, P. Deformation of surfaces due to surface forces. *J. Phys. Chem.* **1992**, *96*, 10398-10405.
16. Attard, P.; Parker, J. L. Deformation and adhesion of elastic bodies in contact. *Phys. Rev. A* **1992**, *46*, 7959-7971.
17. Hertz, H. Ueber die Beruhrung fester elasticher korper. *Reine Angew. Mathematik* **1881**, *92*, 156-171.
18. Derjaguin, B. V.; Muller, V. M.; Toporov, Y. P. Effect of contact deformations on the adhesion of particles. *J. Colloid Interface Sci.* **1975**, *53*, 314-326.
19. Johnson, K.L.; Kendall, K.; Roberts, A.D. Surface energy and the contact of elastic solids. *Proc. R. Soc. Lond. A* **1971**, *324*, 301-313.
20. Attard, P. Interaction and deformation of viscoelastic particles. 2. Adhesive particles. *Langmuir* **2001**, *17*, 4322-4328.
21. Israelachvili, J. N. Intermolecular & Surface Forces 2nd Ed. **1992**, *Academic Press (Boston)*.
22. Argento, C.; French, R. H. Parametric tip model and force-distance relation for Hamaker constant determination from atomic force microscopy. *J. Appl. Phys.* **1996**, *80*, 6082-6090
23. Streator, J. L. An approximate analytical model for the separation of a sphere from a flat in the presence of a liquid. *J. Tribol.* **2006**, *128*, 431-435.
24. Veijola, T.; Kuisma, H.; Lahdenperä, J.; Ryhänen, T. Equivalent-circuit model of the squeezed gas film in a silicon accelerometer. *Sens. Actuat. A* **1995**, *48*, 239-248.
25. Hocking, L. M. Effect of slip on motion of a sphere close to a wall and of two adjacent spheres. *J. Eng. Maths* **1973**, *7*, 207-221.

26. Davis, R. H.; Serayssol, J-M.; Hinch, E. J. The elastohydrodynamic collision of two spheres. *J. Fluid Mech.* **1986**, *167*, 479-497.
27. Darling, R. B.; Hivick, C.; Xua, J. Compact analytical modelling of squeeze film damping with arbitrary venting conditions using a Green's function approach. *Sens. Actuat. A* **1998**, *70*, 32-41.
28. Duffy, D. G. Green's Functions With Applications **2001**, *CRC Press (Boca Raton)*.
29. Morse, P. M.; Feshbach, H. Methods of Theoretical Physics **1953**, *McGraw- Hill (New York)*.
30. Edwards, S. A.; Ducker, W. A.; Sader, J. E. Influence of atomic force microscope cantilever tilt and induced torque on force measurements. *J. Appl. Phys.* **2008**, *103*, 064513.
31. Shampine, L. F.; Reichelt, M. W. The Matlab ODE suite. *SIAM J. Sci. Comp.* **1997**, *18*, 1-22.
32. Bowen, J.; Cheneler, D.; Walliman, D.; Arkless, S. G.; Zhang, Z.; Ward, M. C. L.; Adams, M. J. On the calibration of rectangular atomic force microscope cantilevers modified by particle attachment and lamination. *Meas. Sci. Technol.* **2010**, *21*, 115106.
33. Haynes, W. M.; Lide, D. R. (Eds) CRC Handbook of Chemistry and Physics 92nd Edition **2011**, *CRC Press (Boca Raton)*.
34. Forcada, M. L.; Arista, N. R.; Gras-Martí, A.; Urbassek, H. M.; Garcia-Molina, R. Interaction between a charged or neutral particle and a semi-infinite nonpolar dielectric liquid. *Phys. Rev. B* **1991**, *44*, 8226-8232.
35. Forcada, M. L.; Jakas, M. M.; Gras-Martí, A. On liquid-film thickness measurements with the atomic-force microscope. *J. Chem. Phys.* **1991**, *95*, 706-708.
36. Bowen, J.; Cheneler, D.; Andrews, J.W.; Avery, A.R.; Zhang, Z.; Ward, M.C.L.; Adams, M.J. Application of colloid probe atomic force microscopy to the adhesion of thin films of viscous and viscoelastic silicone fluids. *Langmuir* **2011**, *27*, 11489-11500.
37. Bowen, J; Cheneler, D.; Robinson, A.P.G. Direct e-beam lithography of PDMS. *Microelectronic Eng.* **2012**, *97*, 34-37.
38. Jones, R.; Pollock, H.M.; Cleaver, J.A.S.; Hodges, C.S. Adhesion forces between glass and silicon surfaces in air studied by AFM: Effects of relative humidity, particle size, roughness, and surface treatment *Langmuir* **2002**, *18*, 8045-8055.

Nomenclature

a_T	tip acceleration
$b(x)$	beam shape
c	jump-to separation distance for two spherical surfaces
dL	distance from end of beam to centre of mass of sphere or cone tip
g	acceleration due to gravity
h	Planck's constant
h_1	pyramidal tip height to blunt end
h_2	pyramidal tip height to apex
k	beam spring constant
k_B	Boltzmann's constant
k_{mn}	eigenvalues
ℓ	mean free path length of air
m	integer
m_{EFF}	effective mass of tip and beam
m_{EFFP}	effective mass of pyramidal tip and beam
m_{EFFS}	effective mass of spherical colloid probe tip and beam
n	integer
n_i	refractive index of material i
p	pressure
r	radial distance
s	pyramidal tip base length
t	time
t_0	initial time
u_{mn}	eigenfunctions
$u(r,z)$	profile of deformed surface
$u(r,0)$	deformation of surface underneath the lowest point of the tip
w	beam width
x	distance along beam length
y	distance along beam width
z	vertical distance
A	Hamaker constant between two surfaces
C	jump-to distance
D	separation distance between flat surface and sphere
D_0	mean instantaneous separation distance
$\dot{D}_{FIXED}$	fixed end drive velocity
$\dot{D}_T$	tip velocity
E_S	Young's modulus of substrate
E_B	Young's modulus of beam
E_S^*	reduced modulus of substrate
F	applied force normal to the substrate
F_{IB}	beam inertia
F_{IT}	acceleration of the tip
F_{ITS}	acceleration of a sphere tip
F_{ITP}	acceleration of a pyramidal tip
F_{SB}	force on beam due to fluid squeezing
F_{ST}	force on tip due to fluid squeezing
F_V	van der Waals force between tip and surface
F_{VC}	van der Waals force between a cone and a flat surface
F_{VS}	van der Waals force between a sphere and a flat surface
F_{WB}	weight of the beam
F_{WT}	weight of the tip
F_{WTS}	weight of a sphere tip

F_{WTP}	weight of a pyramidal tip
F'	applied force perpendicular to the free end of the cantilever
$G(\boldsymbol{r}, t\|\boldsymbol{r}_0, t_0)$	Green's function
H	normalised local variation in separation distance
H_0	initial tip position
H_S	substrate hardness
I	moment of inertia of the beam
J	distance between neutral axis and point of force application
K	complete elliptic integral of the first kind
L	beam length
P	normalised local variation in pressure
P_A	ambient pressure
R	sphere radius
R_A	average roughness
R_Z	peak-to-valley roughness
T	torque
T_{CEN}	torque acting on centre of tip
T_{SQ}	torque due to squeeze flow between tip and surface
T_{TOTAL}	total torque
T	temperature
V_0	initial volume
W	beam weight taking into account tilt angle
α	angle of force with respect to the cantilever normal
β	equilibrium angle between vertical axis and cantilever normal
δ	cantilever deflection
ε_i	static dielectric constant of material i
η	constant
θ	angle of cantilever tilt near fixed end
μ	air viscosity
μ_{EFF}	effective air viscosity due to compression
ν_S	Poisson's ratio
ρ_B	beam density
ρ_F	fluid density
ρ_T	tip density
τ	beam thickness
υ_e	plasma frequency of free electron gas
ϕ	cone angle
Kn	Knudsen number
$\Theta(t)$	unit step function
Υ	instantaneous tip position